Attenuation of 7 GHz surface acoustic waves on silicon

Dongyao Li* and David G. Cahill

Department of Materials Science and Engineering, Materials Research Laboratory, University of Illinois, Urbana, Illinois 61801, USA and International Institute for Carbon Neutral Energy Research (WPI-I2CNER), Kyushu University, 744 Moto-oka, Nishi-ku, Fukuoka 819-0395, Japan

(Received 12 December 2015; revised manuscript received 12 July 2016; published 26 September 2016)

We measured the attenuation of GHz frequency surface acoustic waves (SAWs) on the Si (001) surface using an optical pump-probe technique at temperatures between 300 and 600 K. SAWs are generated and detected by a 700 nm Al grating fabricated by nanoimprint lithography. The grating for SAW generation is separated from the grating for SAW detection by ≈150 μm. The amplitude of SAWs is attenuated by coupling to bulk waves created by the Al grating, diffraction due to the finite size of the source, and the intrinsic relaxational Akhiezer damping of elastic waves in Si. Thermal phonon relaxation time and Grüneisen parameters are fitted using temperature-dependent measurement. The fQ product of a hypothetical micromechanical oscillator limited by Akhiezer damping at this frequency is $\sim 3\times 10^{13}$ Hz.

DOI: 10.1103/PhysRevB.94.104306

I. INTRODUCTION

In nonmetallic crystals, the intrinsic attenuation of acoustic waves is governed by the interactions with thermally excited phonons mediated by the anharmonicity of the interatomic potentials [1]. This intrinsic attenuation imposes an upper limit to the quality factor Q of mechanical oscillators, where Q is defined as 2π times the ratio between total stored energy and energy dissipated per cycle of oscillation. The widely used mechanical oscillators such as microelectromechanical systems (MEMS) and nanoelectromechanical systems (NEMS) can now operate at GHz frequencies. High Q factors are needed for their applications as filters and sensors [2–4]. Near room temperature, the Q is typically limited by a multiphonon relaxation process where the strain of the acoustic wave disturbs the distribution of thermally excited phonons, and the relaxation of the distribution to an equilibrium requires an increase of entropy and therefore causes dissipation of energy from the acoustic wave.

Acoustic attenuation by the relaxation of the thermal phonon distribution was first proposed by Akhiezer [5] under the constraint $\omega\tau \ll 1$, where ω is the angular frequency of an acoustic wave and τ is the time scale over which the distribution of thermally excited phonons relaxes to local equilibrium, i.e., the average phonon relaxation time. The theory was later extended using Boltzmann theory [1,6,7] to higher acoustic wave frequencies, $\omega\tau > 1$. Maris [1] pointed out that the Akhiezer theory, or the Boltzmann theory, should be applicable when $\omega \ll k_B T/\hbar$ and $\omega\tau \gg 1$ is satisfied, where T is temperature. Throughout the paper, we will call the attenuation from relaxation of thermally excited phonon at this frequency regime "Akhiezer damping." This definition of the range of applicability of the Akheizer theory is less restrictive than the limit $\omega\tau \ll 1$, which is referred to as the Akhiezer regime in much of the scientific literature on this topic.

A simplified expression for the acoustic attenuation α due to Akhiezer damping is [8–11]

$$\alpha = \frac{CT}{2\rho v^3}\frac{\omega^2\tau}{1+\omega^2\tau^2}(\langle\gamma^2\rangle - \langle\gamma\rangle^2), \tag{1}$$

where C is the volumetric heat capacity, ρ is the density, v is the speed of the acoustic wave, and γ is the mode Grüneisen parameter of the thermally excited phonons; γ depends on the frequency and polarization of the phonon and the mode of the strain. The angular brackets in Eq. (1) denote an average over the entire population of thermally excited phonons. In Sec. IV, we discuss the condition when Eq. (1) is a good approximation to Boltzmann theory.

At low frequencies, $\omega^2\tau^2 \ll 1$, Eq. (1) has a simple quadratic dependence on the frequency of the acoustic wave [1,6]:

$$\alpha = \frac{CT}{2\rho v^3}\omega^2\tau(\langle\gamma^2\rangle - \langle\gamma\rangle^2). \tag{2}$$

This relationship can also be described by a phenomenological equation [12,13]:

$$\alpha = \omega^2\eta/2\rho v^3, \tag{3}$$

where η is the effective phonon viscosity. For a bulk acoustic wave, η can be calculated by the phonon viscosity tensor [13], which has the same symmetry as the elastic constant tensor of the material. Comparing Eqs. (2) and (3), η contains information of both τ and mode Grüneisen parameters and depends on the mode (normal or shear), polarization, and direction of propagation of the acoustic wave. The ideal quality factor Q of an acoustic wave is $Q = \omega/(2\alpha v)$. Therefore, based on Eq. (3), the fQ product is independent of frequency; fQ is often used as a figure of merit [14] for mechanical oscillators.

The highest frequencies achieved in previous studies [8,15–19] of attenuation of an acoustic wave in Si at room temperature is ≈2 GHz. If we estimate $\tau \sim 20$ ps [20], then $\omega\tau \sim 0.2$ and it adequately satisfies the condition $\omega^2\tau^2 \ll 1$. Therefore, in the previous work, Eq. (3) is a good approximation, α has a quadratic dependence on frequency, and the effective phonon viscosity can be obtained from the proportionality between attenuation and ω^2. As we discuss below, previous results for the attenuation of acoustic waves in Si show significant discrepancies. Similarly, data for the phonon viscosity tensor also have large discrepancies [13,16].

None of the previous studies of Si near RT are at frequencies high enough to separate τ and the mean-square variations in

*dli10@illinois.edu

the mode Grüneisen parameters that appear in Eq. (1). When an acoustic wave in Si is at several hundreds of MHz and experiment is done at temperature much lower than Debye temperature, $\omega\tau \sim 1$ is satisfied [8,9] and Eq. (1) has been used to describe the low-temperature measurements. At low temperatures, only a small fraction of the phonon modes in acoustic branches are thermally excited. Since the majority of phonon modes of Si are thermally excited at RT, the low-temperature measurements cannot be reliably extrapolated to RT.

Daly *et al.* [20] recently used Eq. (1) to characterize the attenuation of a longitudinal acoustic wave in Si when $\omega\tau \sim 1$. At RT, the measured attenuation at 50 and 100 GHz is consistent with the assumption of $\langle\gamma^2\rangle - \langle\gamma\rangle^2 = 1$ and fitting of the data with $\tau \approx 20$ ps. Since both the relaxation of the thermal phonon and the Grüneisen parameters are dependent on the acoustic mode, the purpose of the present study is to better understand the Akhiezer damping of acoustic modes with predominately *transverse* polarization when $\omega\tau \sim 1$ at RT. When Eq. (1) is applicable, Q reaches a minimum at $\omega\tau = 1$. We use the temperature dependence of the attenuation in the regime $\omega\tau \sim 1$ to derive estimates of both the thermal phonon lifetime τ and the mean-squared variation of the Grüneisen parameters.

An elastically anisotropic metal film can be used to generate a high-frequency transverse acoustic wave through heating by a short duration optical pulse, but the efficiency is relatively low [21]. We have chosen instead to use a more experimentally convenient approach of measuring the attenuation of surface acoustic waves (SAWs). We show in Sec. III A that the attenuation of SAWs can be connected to Akhiezer damping of bulk transverse acoustic waves. Since pure shear strain in a cubic crystal such as Si does not suffer from thermoelastic damping, we can safely ignore thermoelastic damping in our analysis.

SAWs can be generated and detected in optical pump-probe measurements by providing a spatially periodic source of heat and providing a method for detecting oscillations of strain with the same spatial frequency. The transient grating method [22] uses the interference of two coherent laser beams to create a spatially periodic heat source with a minimum wavelength that is on the order of the wavelength of light. The detection of SAWs in a thermal grating experiment typically involves mixing the scattered wavefront with a carrier, i.e., heterodyne detection [23]. We previously introduced an approach to generate and detect the SAW using a elastomeric phase-shift mask in a conventional pump-probe system [24]. This approach is a convenient method for measurement of elastic constants of thin layers. Unfortunately, however, the elastomeric mask in contact with the sample produces strong damping and an attenuation length on the order of 10 μm. The third approach is to microfabricate a metal grating on the surface of the sample [25–27]. Typically, the pattern of metal bars attenuates the SAW significantly by coupling the SAW to bulk acoustic modes, as we discuss in Sec. III below. By spatially separating the gratings used to generate and detect the SAW, we can minimize and quantify damping created by the grating, and we can probe the intrinsic acoustic attenuation.

The attenuation of SAWs in the context of SAW devices has been discussed previously by Slobodnik *et al.* [28,29]. We provide additional analysis of the intrinsic and extrinsic damping of SAWs.

II. EXPERIMENT

A. Microfabrication of the Al grating structure

The geometry of our sample is shown in Figs. 1(a) and 1(b). An Al grating is fabricated on the (001) surface of an intrinsic Si wafer with a gap of various widths (10–150 μm for every 10 μm) between the regions of grating used to generate and detect SAWs. Figure 1(a) shows a part of the sample with three different width of the gap between generation and detection gratings. This experimental design resembles SAW delay lines used for signal processing and sensing.

Microfabrication of the structure consists of two main steps. First, we define the gap region by standard liftoff techniques. AZ-5214E photoresist is used in image reversal mode to cover the gap region and form a negative wall profile. Then, a thin Al layer (∼15 nm) is sputtered onto the sample surface. After deposition, the photoresist pattern together with the Al film is lifted off by acetone, leaving the gap region uncovered by Al. Second, we define the Al grating by nanoimprint lithography [30,31] due to its ability to generate large pattern areas with high throughput. In nanoimprint lithography, the pattern is transferred from a stamp to the sample by deforming a thin resist layer on the sample by pressing the stamp into the resist layer. Figure 2 shows the flow chart of the full process.

The stamp we use is made of polydimethylsiloxane (PDMS), with a layer of stiffer PDMS (hard-PDMS)

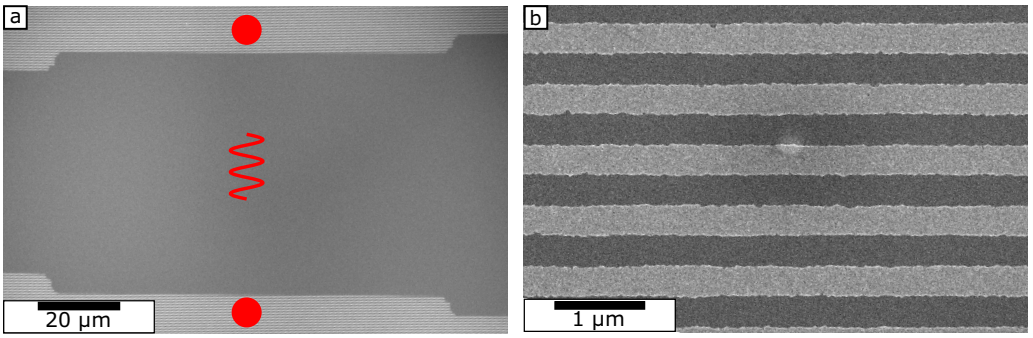

FIG. 1. SEM image of the grating structure. In (a), the dark area is exposed Si. The bright area is the Al grating. Al metal bars are fabricated parallel to the edge of the gap region. Two red points illustrate schematically how the pump and probe beams are separated. In our experiments, the pump and probe beams are separated by 150 μm. The red wavy line indicates the wave propagation from pump grating to probe grating. (b) Higher magnification image of the Al grating with a 700 nm period, ≈15 nm thickness, and ≈50% filling factor.

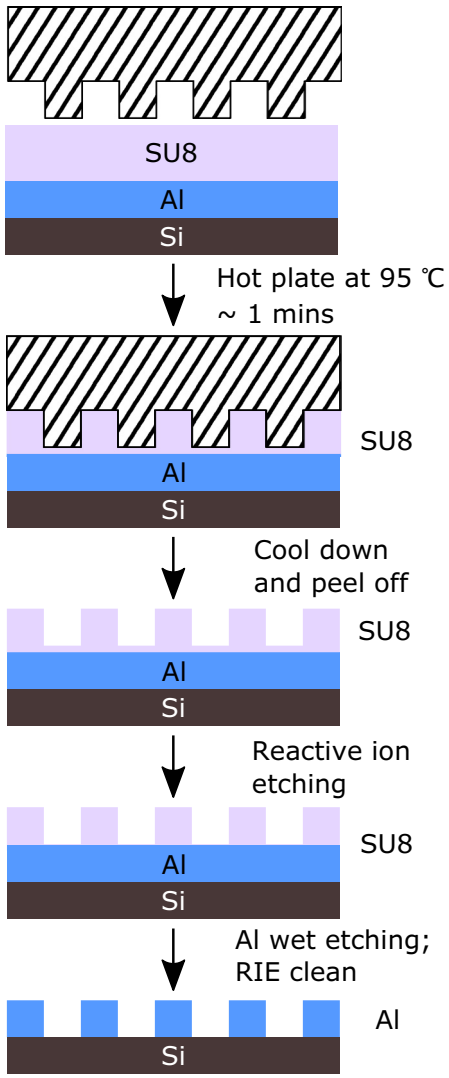

FIG. 2. Process flow diagram for the fabrication of Al gratings using nanoimprint lithography.

on the grating side of the stamp. This so-called "hard-PDMS" is made by mixing trimethylsiloxyterminated vinylmethylsiloxane-dimethylsiloxane (VDT-731, Gelest) and methylhydrosiloxane-dimethylsiloxane (HMS-301, Gelest) copolymers [32]. To make a stamp, the hard-PDMS is first cast and cured (80 °C, about 6 min) on a commercial silicon grating mold (LightSmyth Technology). Then conventional PDMS (Sylgard 184, Dow Corning) is cast and cured (80 °C, 2 h) on top of the hard-PDMS. After curing, the stamp is peeled off and used for nanoimprint lithography. The commercial silicon mold has 700 nm periodicity, ≈50% duty cycle, and 350 nm groove depth.

To prepare the sample for nanoimprint lithography, we spin-coat (2000 rpm for 30 s) SU-8 monomer solution (6% SU-8 monomer in Cyclopentanone) on top of the Al film, followed by curing at 65 °C for 1 min and 95 °C for 1 min successively on a hot plate. The glass-transition temperature of the SU-8 monomer film is ≈95 °C. Finally, the PDMS stamp is placed on top of the sample, on a 95 °C hot plate. The weight of the stamp is sufficient to press the stamp into the resist; i.e., no external force is needed. After ≈1 min, the sample is cooled to room temperature and the stamp is peeled off.

We use reactive ion etching (RIE) to remove the thin SU-8 regions and expose the Al underneath without etching through the thick SU-8 regions. The RIE tool parameters are an oxygen pressure of 100 mTorr, rf power of 100 W, and 20 s etching time. The exposed Al is chemically etched (Al etchant D, Transene) at room temperature for approximately 100 s. Finally, the remaining SU-8 is removed using RIE (100 mTorr oxygen, 400 W rf power, 5 min). Figure 1(b) shows a SEM image of the final grating structure.

The filling factor, i.e., the ratio between the width of the metal bars and the periodicity of the grating, can be controlled by controlling the time of Al wet etching. Al grating with 50% and 35% filling factors has been fabricated, and the effect of the filling factor is discussed in Sec. III C.

B. Generation and detection of SAWs using a metal grating

Generation and detection of SAWs by optical pump-probe techniques has been discussed previously [33]. When the pump optical pulse arrives at the sample surface, the temperature of Al bars rises quickly while the temperature of Si substrate remains relatively unchanged. The expansion of Al causes spatially modulated stress and generates SAWs. The amplitude of SAWs is therefore proportional to the temperature rise of the Al, which is proportional to the average power of the pump beam.

In many experiments that probe SAWs optically, SAWs scatter light due to surface displacements rather than elasto-optic coupling [34]. For the specific case of our Al grating structure, the electric field reflected by the Al regions of the sample is larger than the electric field reflected from the bare Si regions of the sample. The perpendicular displacements of the Al bars are in phase with each other when the wavelength of the SAW is equal to the periodicity of the Al grating. The modulation of the reflected electric field is therefore linear in the displacements, and the modulation of the reflectivity is proportional to the SAW amplitude. By contrast, the scattering cross section of SAWs on a grating-free surface is quadratic in the SAW amplitude [34]. In our experiments, the amplitude of the detected signal scales linearly with the pump power, as expected.

Our pump-probe system is described in Ref. [35]. The laser has a repetition rate of ≈74 MHz. The output is split into a probe pulse and a pump pulse. Each pump pulse excites a SAW wave packet. The probe can be delayed relative to the pump by up to ≈4 ns. Each probe pulse can detect SAW wave packets generated by any previous pump pulse; for example, if the delay line is set to 2 ns, then the probe pulses can detect SAWs that have propagated for 2, 16, 30, 44 ns, etc. We use spatially separated pump and probe optical pulses to detect SAWs that have propagated relatively long distances to increase the sensitivity of the experiment to the intrinsic SAW attenuation.

We label the pump pulse that is split off from the given probe pulse as pump pulse $n = 0$, the prior pump pulse to be $n = -1$, the pulse before that to be $n = -2$, etc. We modulate the pump beam at ≈9.3 MHz (1/8 of the laser repetition rate) and synchronously detect the modulation of the reflected

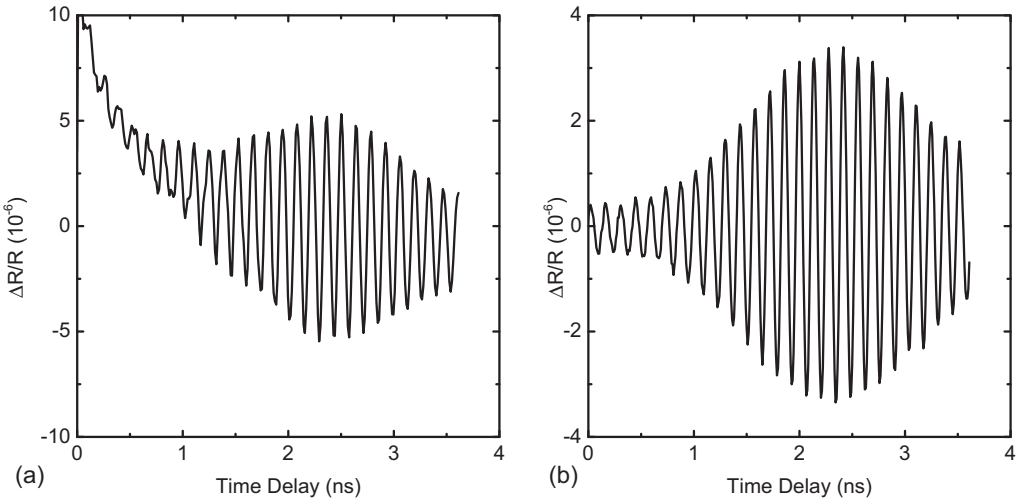

FIG. 3. (a) Typical in-phase signal for a close offset measurement. Pump and probe beams are offset by 10 μm. (b) Typical out-of-phase signal for a far offset measurement. Pump and probe beams are offset by 150 μm.

probe intensity with a fast photodiode and rf lock-in amplifier. Detection of the SAW wave packet generated by pump pulse n has an $\approx -n\pi/4$ phase difference with respect to the reference signal.

In Sec. III C, we discuss how the grating structure with a non-50% filling factor creates a band gap at the Brillouin-zone center. Since we cannot make the grating with exactly 50% filling factor, there is always a small band gap at the Brillouin-zone center. This band gap produces components with small group velocity. These minor components of the signal will trail behind the wave packet. Each response to a pump optical pulse is overlapped by the trailing part of the response to the previous pump pulse because the current response can catch up with the low group velocity component of the previous response.

To measure attenuation, we need to separate the responses; the phase shifts described above help accomplish that task. We set the spatial offset between the pump and probe beams at $\approx$150 μm, which corresponds to the position of SAW packets generated by pump pulse $n = -2$. The signal has a $\pi/2$ phase shift and appears only in the out-of-phase channel. The response from pump $n = -3$ will appear in both the in-phase and out-of-phase channel. Since we observe that the in-phase signal is negligible compared with the out-of-phase signal, we conclude that the out-of-phase signal is not significantly contaminated by a contribution from pump $n = -3$.

Figure 3(a) shows the typical signal for a small offset between pump and probe, and Fig. 3(b) shows the typical signal for a large offset. By comparing the amplitude of the Gaussian wave packet as a function of beam offset, we can determine the attenuation.

III. PROPERTIES OF SAW ON A SILICON WITH METAL GRATING

To better estimate the intrinsic SAW attenuation of Si, we must consider and correct for additional mechanisms that cause the wave amplitude to change with distance of propagation. In the following sections, we consider the effect of the mass of the Al grating and diffraction of the acoustic wave.

A. SAW on a Si (100) plane

Using a Green's-function method [36], we calculate the dispersion of SAWs of the bare substrate and the substrate patterned with a thin metal grating. We define the Cartesian axis where axes $\hat{a}_1$ and $\hat{a}_2$ are in the plane of the surface, and axis $\hat{a}_3$ is perpendicular to the surface. $G_{ij}(k,\omega,x_3)$ is the elastodynamic Green's-function tensor in Fourier space (angular frequency ω and wave vector k of SAW) evaluated at depth x_3. $G_{33}(k,\omega,x_3 = 0)$ is its (3,3) component, which is at the surface $x_3 = 0$ and represents the perpendicular displacement (in the $\hat{a}_3$ direction) with excitation force at the $\hat{a}_3$ direction. $G_{33}(k,\omega,x_3 = 0)$ has the information of the dispersion relation of the SAW, which can be used to calculate SAW velocity. Appendix A describes the details of the calculation.

Our measurements are on the Si (001) surface. For a cubic crystal, SAWs propagating along the $\langle 100\rangle$ or $\langle 110\rangle$ direction are Rayleigh surface acoustic waves (RSAWs), i.e., the sagittal plane of SAWs is perpendicular to the surface [37]. For Si(001), as the propagation direction of the SAW rotates from $\langle 100\rangle$ to $\langle 110\rangle$, the SAW is a Rayleigh-like wave and it gradually converts into the bulk transverse wave with polarization parallel to the surface. The sagittal plane is no longer perpendicular to the surface, but there is no wave energy radiating into the substrate. At directions close to $\langle 110\rangle$, there is very small or no displacement perpendicular to the surface in the Rayleigh-like wave, and it can no longer be measured in our experimental setup. Beyond $\approx 37^\circ$ from $\langle 100\rangle$, another mode called the pseudo surface acoustic wave (PSAW) [38] arises. The PSAW has a wave component that radiates into the bulk. In the $\langle 110\rangle$ direction, the radiating component disappears and the wave becomes RSAW again. What we measured is at $\langle 110\rangle$ and it belongs to the PSAW branch. To simplify the terminology in what follows, we use the term SAW to describe both PSAWs and SAWs.

We calculate the SAW velocity (v_{SAW}) using elastic constants of Si [39]: $c_{11} = 167.4$ GPa, $c_{12} = 65.2$ GPa $c_{44} = 79.6$ GPa, and density $\rho = 2.33$ g/cm^3. At the $\langle 110\rangle$ direction where the measurements are carried out, $v_{\mathrm{SAW}} = 5.09$ nm/ps. The SAW in our experiment has 700 nm wavelength. Thus,

the predicted frequency is $f = 7.27$ GHz or, equivalently, an angular frequency of $\omega = 45.7$ s^{-1}. Experimentally, we observe $f = 7.17$ GHz. We attribute the 1.3% difference to the mass of the patterned Al grating. From linear-response theory, $\mathrm{Im}(G_{33}(k,\omega,x_3 = 0))$ arises because of dissipation. The width of $\mathrm{Im}(G_{33}(k,\omega,x_3 = 0))$ in the frequency coordinate can be used to infer the quality factor Q of the SAW created by coupling to bulk acoustic waves. From our calculations, we find that for a propagation direction within 5° of ⟨110⟩ direction, the Q factor is $>3\times10^4$ due to radiation of acoustic energy into the bulk, and therefore we can neglect this mechanisms for attenuation of the PSAW.

We calculate the symmetric strain tensor ϵ_{ij} with $i,j = 1,2,3$ in the SAW at the (001) plane and propagating in the ⟨110⟩ direction. The amplitude of the density of elastic energy is $E_{\mathrm{el}} = \frac{1}{2}c_{ijkl}\epsilon_{ij}\epsilon^*_{kl}$. The strain is represented by a complex number, and an asterisk denotes complex conjugate. For cubic crystals, the nine components of the symmetric strain tensor can be viewed as the basis of the representation of the group, which is the symmetrized product of the point group of the cubic crystal [40–42]. The resulting group is reducible; therefore, the six independent components of strain tensor can be recombined to form the new basis of the three irreducible representations. The volumetric strain mode $\epsilon_v = \epsilon_{11} + \epsilon_{22} + \epsilon_{33}$ corresponds to the bulk modulus $c_B = (c_{11} + 2c_{12})/3$; the two equivalent stretch modes $\epsilon_2 = \epsilon_{11} - \epsilon_{22}$ and $\epsilon_3 = (2\epsilon_{33} - \epsilon_{11} - \epsilon_{22})/\sqrt{3}$ correspond to tetragonal shear modulus $(c_{11} - c_{12})/2$; and three equivalent shear modes ϵ_{12}, ϵ_{13}, and ϵ_{23} correspond to shear modulus c_{44}. The density of elastic energy in a cubic crystal is then [42,43]

$$E_{el} = \frac{1}{2}c_B|\epsilon_v|^2 + \frac{c_{11} - c_{12}}{4}(|\epsilon_2|^2 + |\epsilon_3|^2) + 2c_{44}(|\epsilon_{12}|^2 + |\epsilon_{13}|^2 + |\epsilon_{23}|^2). \quad (4)$$

When $\omega^2\tau^2 \ll 1$ is satisfied, the concept of phonon viscosity can be applied to calculate the Akhiezer damping of SAWs as described by Maris [44]. We adopt part of Maris's approach and provide a brief derivation of the effective viscosity of SAWs in the following. The average rate of energy loss, P_v, due to phonon viscosity is [44]

$$P_v = \frac{1}{2}\omega^2 \int \eta_{ijkl}\epsilon_{ij}\epsilon^*_{kl}\, dV, \quad (5)$$

where η_{ijkl} is the phonon viscosity tensor and the integral is over volume. The total energy of the SAW is the same as the amplitude of the elastic energy, since the time average of elastic energy and kinetic energy is the same. Therefore, the total energy of the system is

$$W = \int E_{\mathrm{el}}\, dV. \quad (6)$$

Since the phonon viscosity tensor η_{ijkl} has the same symmetry as elastic constants tensor c_{ijkl}, the average rate of energy loss by Akhiezer damping in Si is

$$P_v = \int \omega^2\left[\frac{1}{2}\eta_B|\epsilon_v|^2 + \frac{\eta_{11} - \eta_{12}}{4}(|\epsilon_2|^2 + |\epsilon_3|^2) + 2\eta_{44}(|\epsilon_{12}|^2 + |\epsilon_{13}|^2 + |\epsilon_{23}|^2)\right] dV, \quad (7)$$

where $\eta_B = (\eta_{11} + 2\eta_{12})/3$. By writing the attenuation coefficient as

$$\alpha_{\mathrm{SAW}} = \frac{P_v}{2W v_{\mathrm{SAW}}} = \frac{\omega^2\eta_{\mathrm{SAW}}}{2\rho v^3_{\mathrm{SAW}}}, \quad (8)$$

the effective viscosity of the SAW can be defined as

$$\eta_{\mathrm{SAW}} = \frac{\rho v^2_{\mathrm{SAW}}}{2W}\int\left[\eta_B|\epsilon_v|^2 + \frac{\eta_{11} - \eta_{12}}{2}(|\epsilon_2|^2 + |\epsilon_3|^2) + 4\eta_{44}(|\epsilon_{12}|^2 + |\epsilon_{13}|^2 + |\epsilon_{23}|^2)\right] dV. \quad (9)$$

For the SAW on the Si (001) surface along the ⟨110⟩ direction, the effective viscosity is

$$\eta_{\mathrm{SAW}} = 0.059\eta_B + 0.269\left(\frac{\eta_{11} - \eta_{12}}{2}\right) + 0.545\eta_{44}, \quad (10)$$

where η_{44} is the effective viscosity of a fast transverse (FT) bulk acoustic wave in the ⟨110⟩ direction, and $(\eta_{11} - \eta_{12})/2$ is the effective viscosity of a slow transverse (ST) bulk acoustic wave in the ⟨110⟩ direction. Thus, the SAW attenuation in our measurements has predominantly shear character.

B. Diffraction and phonon focusing

The SAW is generated by a pump laser beam with a $1/e^2$ spot size of $w_0 = 5.5$ μm. The propagation distance that separates the near-field from the far-field is on the order of $\pi w_0^2/\lambda$, where λ is the acoustic wavelength. The propagation distance in our experiments (≈150 μm) is comparable to $\pi w_0^2/\lambda \approx 140$ μm, and we must consider diffraction in our data analysis.

We start by considering diffraction of a two-dimensional (2D) wave for an isotropic medium for a wave of wave vector $k = 2\pi/\lambda$. The wave amplitude at an arbitrary position (x_0, y_0) is the superposition of the circular waves generated by each point of the source. For a line source centered at $x = 0, y = 0$ and extending in the y direction with Gaussian intensity distribution $u_0 \equiv \exp(-2y^2/L^2)$ (L is the $1/e^2$ spot radius), the wave amplitude at (x_0, y_0) is

$$U(x_0,y_0) \propto \int_{-\infty}^{\infty} \exp\left(-2\frac{y^2}{L^2}\right)\frac{\exp\left(-ik\sqrt{x_0^2 + (y_0 - y)^2}\right)}{\left[x_0^2 + (y_0 - y)^2\right]^{1/4}} dy. \quad (11)$$

The exponential term in the numerator is the phase of circular waves. The amplitude of a circular wave in two dimensions falls off with distance r as $1/\sqrt{r}$.

The Si (100) surface is not isotropic, and the SAW velocity v_{SAW} varies with direction. We plot the slowness surface $1/v_{\mathrm{SAW}}$ in Fig. 4. From ⟨100⟩ to ≈37° away from ⟨100⟩, the SAW is Rayleigh-like and has relatively big perpendicular displacement (therefore measurable in experiment), and its slowness surface is plotted. Beyond ≈37° until ⟨110⟩, the PSAW has much bigger perpendicular displacement, and its slowness surface is plotted. The discontinuity in Fig. 4 appears because the slowness surface of the two modes does not intersect. The vector normal to the slowness surface is the direction of the group velocity. For directions near ⟨110⟩, the slowness surface has smaller curvature than a circle, and

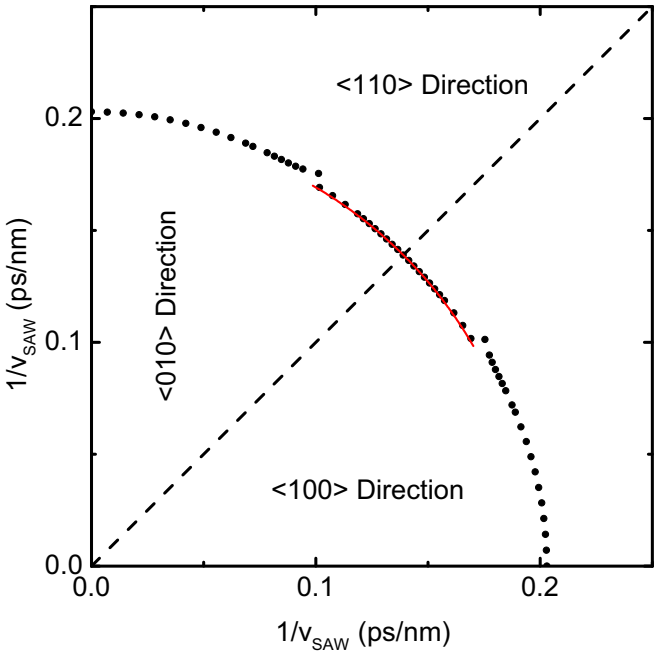

FIG. 4. Slowness surface of the Rayleigh-like SAW (from the ⟨100⟩ direction to ≈37° away, where the discontinuity is located) and the PSAW (from the discontinuity to the ⟨110⟩ direction) on the Si(001) plane, and a comparison between the slowness surface close to the ⟨110⟩ direction and a circle (red line).

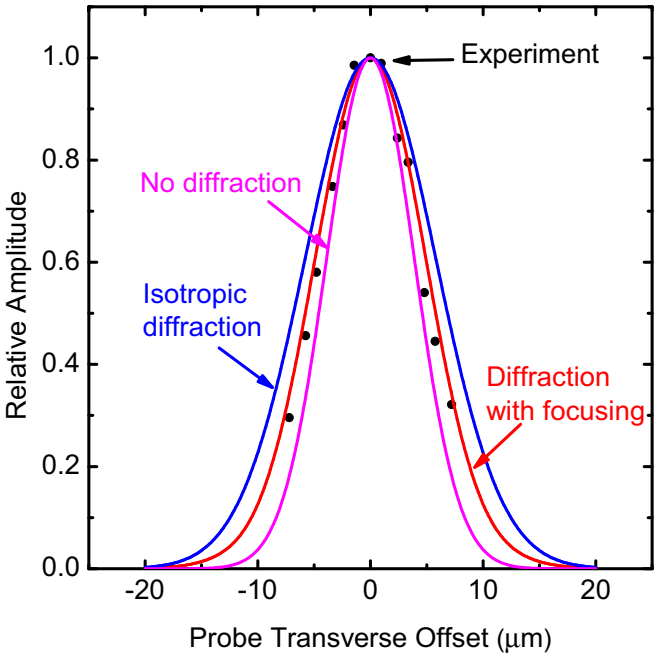

FIG. 5. Relative signal intensity when the probe beam is offset at the transverse direction at far field. Black dots are experiment results. The red line is the calculation considering phonon focusing [Eq. (12)]. The blue line is calculated diffraction for an isotropic plane [Eq. (11)]. The line labeled "No diffraction" is the calculation if no diffraction is considered.

the vectors normal to the slowness surface tilt toward ⟨110⟩. This phonon focusing effect concentrates energy toward ⟨110⟩ and suppresses the effects of diffraction in this direction.

Taking into account phonon-focusing effects, the wave intensity at (x_0, y_0) is [45,46]

$$U(x_0,y_0) \propto \int_{-\infty}^{\infty} \sum_{l=1}^{N} \frac{u_0(y)}{\sqrt{|\bar{r}|}\, v_g^{(l)} \kappa^{(l)}} \exp(-i\bar{k}^{(l)} \cdot \bar{r}) dy, \quad (12a)$$

$$\bar{r} = (x_0, y_0 - y), \quad (12b)$$

$$u_0(y) = \exp(-2y^2/L^2), \quad (12c)$$

$$\bar{n} = \frac{\bar{r}}{|r|}. \quad (12d)$$

To evaluate Eq. (12), we first find $\bar{n}$, the direction vector from point source $(0, y)$ to field point (x_0, y_0). Then we search the slowness surface to find points $s^{(1)}$ to $s^{(N)}$ whose group velocities have the same direction as $\bar{n}$. These N points have group velocity $\bar{v}_g^{(l)}$, phase velocity $\bar{v}_p^{(l)}$, curvature $\kappa^{(l)}$, and wave vectors $\bar{k}^{(l)} = \omega \bar{v}_p^{(l)}$, $l = 1, \ldots, N$. Note that if the slowness surface is a circle, then $\bar{v}_g = \bar{v}_p = \bar{v}$ and only one point would satisfy the requirement.

We experimentally verify this calculation by measuring the wave amplitude as a function of probe position displaced perpendicular to the wave propagation direction, i.e., the transverse direction, at ≈150 μm from the source; see Fig. 5. The calculation for the isotropic case, Eq. (11) (blue line), gives a wider distribution along the transverse direction than experiment. The calculation for the phonon-focusing case, Eq. (12) (red line), is narrower and fits the measurement well.

C. Effect of metal grating

The effect of a thin metal grating on SAWs has been described previously [25,47]. We numerically model the perturbation of SAWs created by the metal grating using the mass loading approximation [47] and the surface Green's-function method. (Details of our calculations are given in Appendix A.) The grating creates changes in dispersion, i.e., band structure, and attenuation, i.e., reduced lifetimes.

Without the grating, the dispersion is a straight line with equal group and phase velocity. When a periodic array of metal bars is added to the surface, these bars are displaced together with the surface by the SAW. The surface must provide sufficient force to drive the displacement of the bars, and therefore the boundary condition at the surface is a periodic force field. Similar to an electron wave function in a periodic potential, the dispersion curves of SAWs are folded into the first Brillouin zone: $-\pi/\lambda$ to π/λ, where λ is the periodicity of the grating.

Because of the folding in k space, the SAW dispersion curve intersects the dispersion curve of fast bulk transverse acoustic waves and bulk longitudinal acoustic waves. The figure in Appendix A 3 shows the dispersion in the first Brillouin zone and coupling between the SAW and the bulk acoustic wave. Al has relatively low density and produces less attenuation than a high density metal such as Au [25].

Zone folding can create a band gap at the Brillouin zone center if the filling factor of the grating deviates from 0.5. Figure 6 plots $\mathrm{Im}(G_{33}(k,\omega,x_3 = 0))$ near the Brillouin zone center with δ excitation. Figure 6(a) shows that if the filling factor is 0.5, there is no band gap at the Brillouin-zone

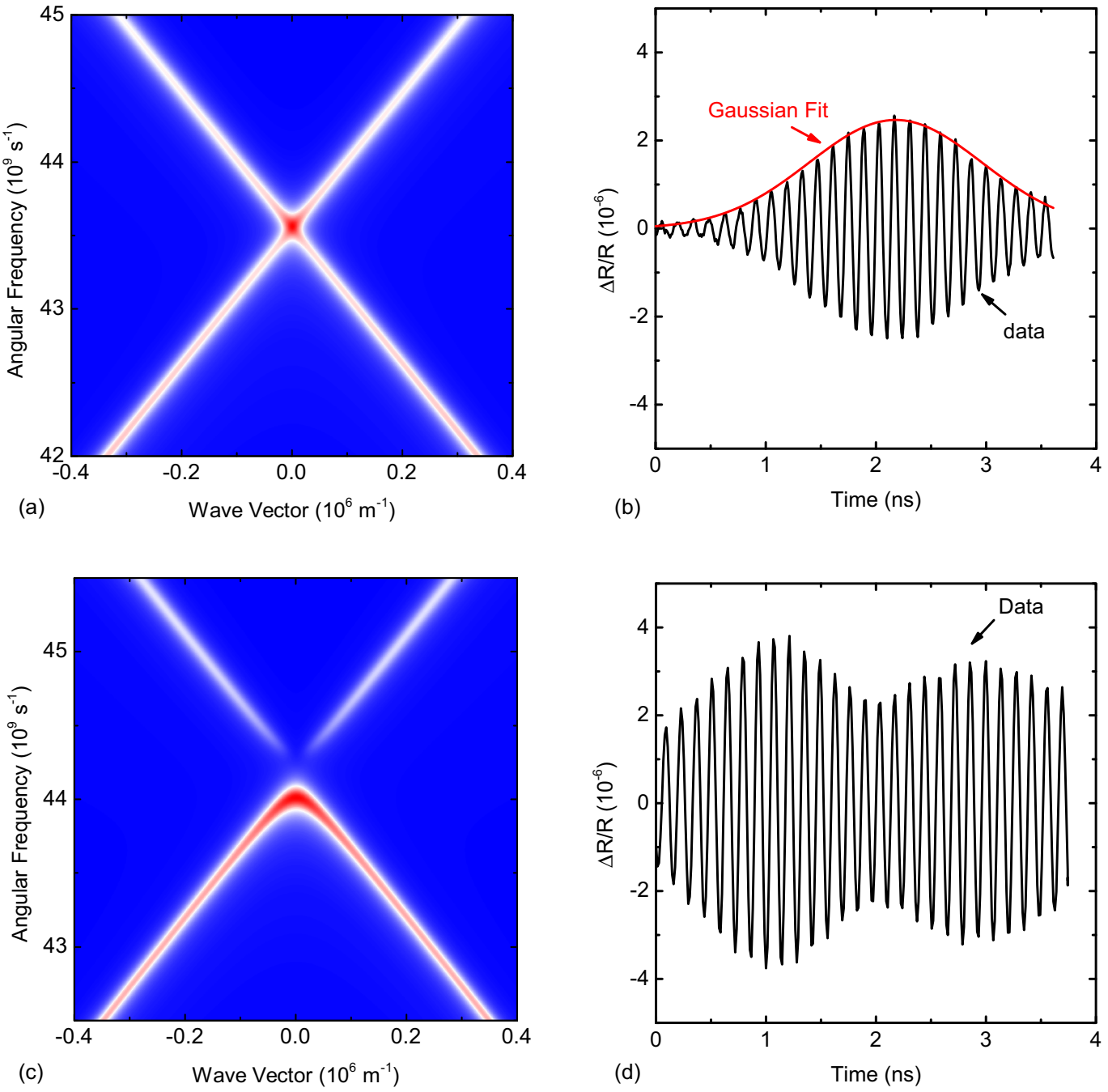

FIG. 6. (a) Im(G_{33}) at the Brillouin-zone center with 0.5 grating filling factor and δ excitation. (b) Far-field signal with grating of $\approx$0.5 filling factor. (c) Im(G_{33}) at the Brillouin-zone center with 0.35 grating filling factor and δ excitation. (d) Far-field signal with grating of $\approx$0.35 filling factor.

center. However, if the filling factor is not 0.5, for example 0.35, as shown in Fig. 6(c), there is a significant band gap at the Brillouin-zone center from $\approx -0.04\times10^6$ m^{-1} to $\approx$0.04$\times10^6$ m^{-1}.

For a filling factor that deviates from 0.5, the $k = 0$ modes of the two branches are standing waves with a $\pi/2$ phase difference. Because of this phase difference, the two standing waves drive the metal bars with different magnitude displacements and accelerations, and the energies of the two waves are different, opening a gap. If the grating has a 0.5 filling factor, standing waves with $\pi/2$ phase difference have the same magnitude of displacement and hence the same energy, and the energy gap at $k = 0$ is zero.

Deviations from a 0.5 filling factor and the opening of a gap at the zone center are important in our measurements. A SAW excited by a finite-size pump beam is composed of wave components over a range of wave vectors k of $-2\pi/L < k < 2\pi/L$ near the Brillouin-zone center, where $L \approx 5.5$ μm is the $1/e^2$ radius of the focused pump. So the range of the excited wave vector is from $\approx -0.18\times10^6$ m^{-1} to $\approx$0.18$\times10^6$ m^{-1}. These components combine to form a Gaussian wave packet. If a band gap exists at the zone center, then the wave components

close to the zone center have suppressed group velocity. After propagating a long distance, these slower components of the wave packet will lag behind the other components of the wave packet, with k farther away from the zone center. For grating with a 0.35 filling factor, ≈20% of the wave component has group velocity ranging from the SAW velocity v_{SAW} to zero (right at the center of the band gap), as Fig. 6(c) shows. Thus, the shape of the wave packet will not be Gaussian, as Fig. 6(d) shows, and is difficult to interpret. If the band gap is small, then the wave packet has a Gaussian shape, as Fig. 6(b) shows, and is simpler to analyze.

IV. RESULT AND DISCUSSION

We define the wave amplitude measured with closely separated (l_{close}) pump and probe as R_{close} and the wave amplitude with widely separated (l_{far}) pump and probe as R_{far}; the total attenuation of SAW after it travels $l = l_{close} - l_{far}$ is $A = R_{far}/R_{close}$. As discussed in Sec. III, A contains effects from diffraction, damping created by the metal grating, and the intrinsic attenuation of Si:

$$A \equiv \frac{R_{far}}{R_{close}} = f(l)D(l)\exp(-\alpha_g l_g)\exp(-\alpha_{Si} l), \qquad (13)$$

where α_{Si} is the intrinsic attenuation coefficient, α_g is the attenuation coefficient of the Al grating, and l_g is the width of the Al grating region. $D(l)$ is the contribution of diffraction and phonon focusing. $f(l)$ is a sum of all the other effects that we are not considering, for example the effect of surface roughness and the presence of the native oxide of Si.

As described in Sec. II B, for R_{far} we want to measure the SAW generated by pump pulse $n = -2$ and place the signal in the out-of-phase channel. We therefore separate the pump and probe by $l_{far} = 147\ \mu$m, which is how far the SAW travels in ≈30 ns. In this way, we position the probe so that the wave packet is at the center of the measurement window. To measure R_{close}, we want to suppress the thermal signal. We choose $l_{close} = 10\ \mu$m so that the thermal signal is small and the SAW wave packet is at the center of the measurement window.

We first consider the amplitude change $D(l)$ caused by diffraction combined with phonon focusing. Calculation using Eq. (12) gives $D(l) = 0.85$.

We then consider damping created by the grating. Experimentally, we find $\alpha_g > \alpha_{Si}$. To increase the sensitivity of the experiment to α_{Si}, we must minimize l_g. Even the grating within the small distance of propagation across the width of the pump and probe optical beams creates appreciable damping, and therefore we must quantify the damping created by the Al grating to improve the measurement of α_{Si}. Based on Eq. (13), $\ln(R_{far}/R_{close})$ changes linearly with l_g. Thus, we can fit a line to $\ln(R_{far}/R_{close})$ versus l_g and extrapolate to $l_g = 0$ to remove damping created by Al grating.

We achieve this by varying the gap width. Figure 1 shows part of the sample that has three different gap widths. In experiment, we change the gap size from 130 to 90 μm, but we keep l_{far} constant, i.e., the width of the grating region varies from 17 to 57 μm. To align the relative position of pump and probe along the transverse direction, we displace the pump beam along the transverse direction and find the position where the signal is maximized.

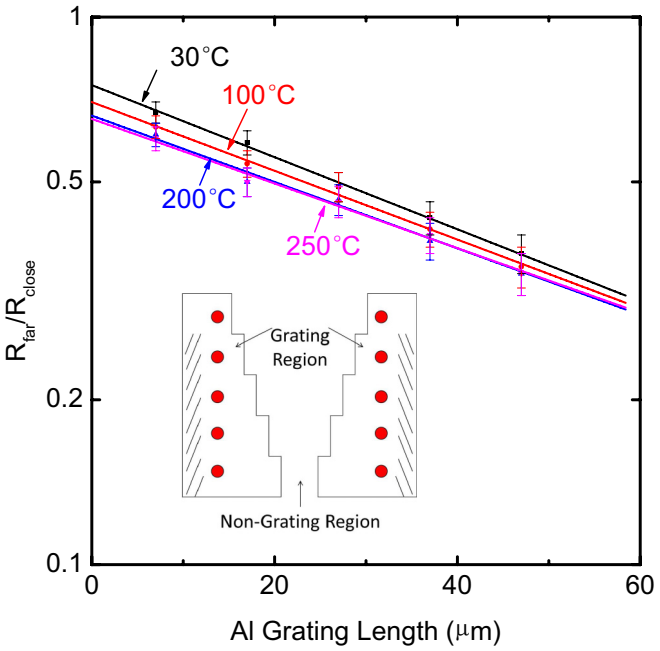

FIG. 7. Ratio between wave amplitudes of far offset and close offset with different lengths of the grating region. The vertical axis is plotted on a log scale, and data are fitted with straight lines. Each set of data is labeled by the sample temperature. The slope can be used to calculate the attenuation coefficient of the Al grating. The inset is the measurement configuration for far offset. Red dots stand for pairs of positions of pump and probe beams. Repeating the measurement for five different gap widths while keeping the distance between the pump and probe beams constant introduces five different lengths of the grating region. Comparing them with the close offset measurement gives five data points at each temperature. The results are extrapolated to zero grating length (on the vertical axis) to get intrinsic attenuation.

The inset of Fig. 7 shows the experimental configuration to measure R_{far}. Figure 7 shows the measured attenuation with five different widths of grating region, fitting, and extrapolation to the point where attenuation from the Al grating is removed. We repeat the measurement at four temperatures: 30, 100, 200, and 250 °C. If $f(l)$ is assumed to be 1, we can obtain the following: at 30 °C, $\alpha_g = 152\ \text{cm}^{-1}$ and $\alpha_{Si} = 9\ \text{cm}^{-1}$; at 100 °C, $\alpha_g = 145\ \text{cm}^{-1}$ and $\alpha_{Si} = 14.2\ \text{cm}^{-1}$; at 200 °C, $\alpha_g = 140\ \text{cm}^{-1}$ and $\alpha_{Si} = 18.4\ \text{cm}^{-1}$; and at 250 °C, $\alpha_g = 136\ \text{cm}^{-1}$ and $\alpha_{Si} = 19.4\ \text{cm}^{-1}$.

In Boltzmann theory, the change in the occupation number of a mode is generated by two processes: phonon transport between regions with different strain, and localized phonon relaxation due to phonon collisions [1]. Equation (1) can be viewed as a result from localized relaxation theory [9], with $Q \propto \omega\tau/(1+\omega^2\tau^2)$. Therefore, Eq. (1) is a good approximation when phonons relax locally before they propagate to regions with different strain, i.e., $\langle v_{phonon}\rangle\tau \ll v/f$, where $\langle v_{phonon}\rangle$ is the averaged group velocity of thermally excited phonons, $f = \omega/2\pi$ is the frequency of the acoustic wave, and v is the velocity of the acoustic wave. This condition can be written as $\omega\tau < v/\langle v_{phonon}\rangle$. At a temperature much

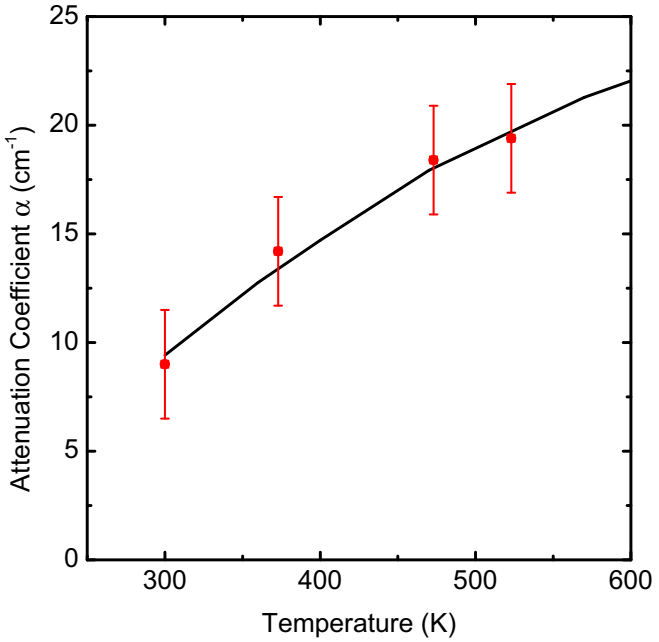

FIG. 8. Temperature dependence of the measured intrinsic attenuation coefficient. Red points are measurements. The black line is a fit to the data using Eq. (1) and $\tau = 30$ ps and $(\langle\gamma^2\rangle - \langle\gamma\rangle^2) = 0.053$.

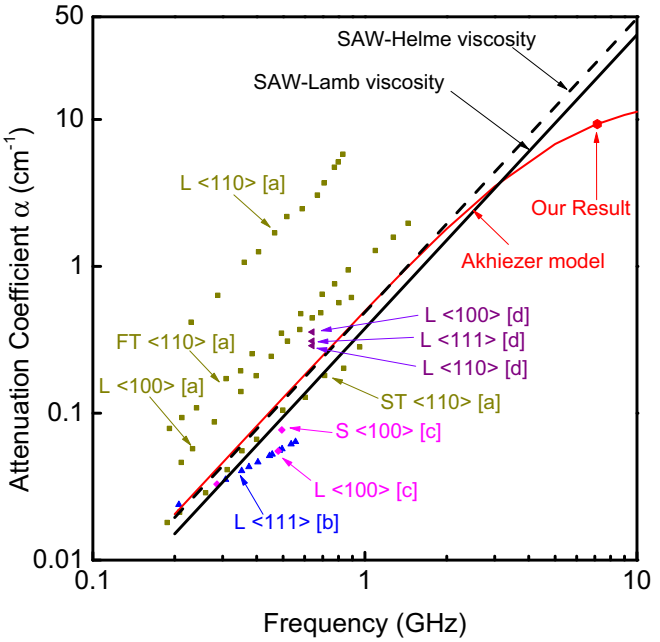

FIG. 9. Comparison between our result and prior reports and the phonon viscosity model. L denotes a longitudinal bulk acoustic wave. FT and ST denote a bulk fast transverse acoustic wave and a bulk slow transverse acoustic wave, respectively. Notation like $\langle 100\rangle$ denotes the propagation direction. Data marked [a] are from Ref. [18], data marked [b] are from Ref. [15], data marked [c] are from Ref. [8], and data marked [d] are from Ref. [19]. The straight line of "SAW-Lamb viscosity" and the dashed line "SAW-Helme viscosity" correspond to the attenuation coefficient of SAW calculated using Eq. (3) and the effective viscosity of SAW from Eq. (10). They use the phonon viscosity tensor from Lamb and Richter [13] and Helme and King [16], respectively. The Akhiezer model is calculated using Eq. (1), where τ and $\langle\gamma^2\rangle - \langle\gamma\rangle^2$ are from our measurement.

lower than the Debye temperature, only a small fraction of the acoustic phonon branches are excited, and $v/\langle v_{\text{phonon}}\rangle \geqslant 1$. Mason *et al.* [8,9] show that Eq. (1) fits the measured acoustic attenuation of Si well at low temperature when $\omega\tau \geqslant 1$. For Si at RT, the majority of phonon modes are excited. The phonon modes with a larger wave vector generally have a smaller group velocity and a higher density of states. In particular, the group velocity of optical phonons is much smaller than v. Thus, we conclude that $v/\langle v_{\text{phonon}}\rangle > 1$ in Si at RT. Our experiment falls into the $\omega\tau \sim 1$ and RT regime, $\omega\tau < v/\langle v_{\text{phonon}}\rangle$ is satisfied, and Eq. (1) is a good approximation.

We fit results for α_{Si} to Eq. (1); see Fig. 8. In Eq. (1), we use the heat capacity for Si from Ref. [48]. We assume that the relaxation time scales as $\tau \propto 1/T$. The fitting gives $\tau = 30$ ps and $\langle\gamma^2\rangle - \langle\gamma\rangle^2 = 0.053$. The experimental uncertainty in τ is large, approximately a factor of 2. The uncertainty in $\langle\gamma^2\rangle - \langle\gamma\rangle^2$ is much smaller, on the order of ± 0.01.

The measured intrinsic attenuation coefficient and Akhiezer model using the fitted τ and $(\langle\gamma^2\rangle - \langle\gamma\rangle^2)$ are compared with previous experimental results and phonon viscosity modeling in Fig. 9, which also reveals discrepancies among prior experiments and the phonon viscosity models.

Based on our analysis of Sec. III A, the attenuation coefficient of the SAW by the theory of phonon viscosity can be calculated by Eq. (3) with the effective viscosity η_{SAW} calculated by Eq. (10). The results using phonon viscosity tensors of Lamb and Richter [13] and Helme and King [16] are labeled as "SAW-Lamb viscosity" and "SAW-Helme viscosity," respectively, in Fig. 9. Extrapolation of our experimental results to $\omega^2\tau^2 \ll 1$ agrees better with the calculation based on Helme and King's phonon viscosity tensor. In the regime of our measurements, $\omega\tau \sim 1$, the Akhiezer damping predicted by Eq. (1) deviates significantly from the phonon viscosity model, Eq. (3).

The energy dissipation in a mechanical oscillator can be from extrinsic and intrinsic mechanisms. Two important extrinsic mechanisms are air damping [49] and clamping loss [50,51]. The intrinsic damping mechanisms are thermoelastic dissipation [3,52] and Akhiezer damping. For extrinsic damping, vacuum packaging can be used to eliminate air damping, and the symmetrical design of a mechanical oscillator can reduce the clamp damping. For intrinsic damping, utilizing specific modes can suppress thermoelastic dissipation. For example, a pure shear strain in cubic crystal does not cause a volume change, and therefore no thermoelastic dissipation occurs. Akhiezer damping is created by a local strain and represents a fundamental upper limit to the Q of mechanical oscillators. Our measurements show that the mean-squared variation of Grüneissen parameters $\langle\gamma^2\rangle - \langle\gamma\rangle^2$ of shear strain is an order of magnitude smaller than the corresponding parameters for normal strain [8,14,53]. Comparing with the Akhiezer damping of a longitudinal acoustic wave measured by Daily *et al.* [20], the Akhiezer damping of an acoustic wave at GHz with predominately shear character is approximately six times smaller. A silicon mechanical oscillator with a vibrational mode of mostly shear character will have a higher upper limit of the Q factor than one with a vibrational mode of predominately normal character.

In summary, we measure the attenuation of 7.2 GHz transverse acoustic waves to be $\alpha_{Si} \approx 9\ \mathrm{cm}^{-1}$ at room temperature. The result of a small mean-squared variation of Grüneissen parameters for shear strain indicates a high-Q factor for a mechanical oscillator with mostly shear character.

ACKNOWLEDGMENTS

This work was done at University of Illinois and was supported by the International Institute for Carbon Neutral Energy Research (WPI-I2CNER), sponsored by the Japanese Ministry of Education, Culture, Sports, Science and Technology. The authors thank Li Gao for her help with sample fabrication.

APPENDIX: CALCULATION OF THE SURFACE GREEN'S FUNCTION

We describe here the procedure of calculation of the surface Green's function of a bare substrate, a substrate with uniform mass loading, and a substrate with periodic mass loading. We adopted the treatment of metal grating in Ref. [47] into the Green's function method described in Ref. [54]. For completeness, we give a full derivation of our calculation.

1. SAW of substrate

We start with the calculation of a bare substrate. For any acoustic waves, the displacement $\bar{U} = [U_1, U_2, U_3]$ satisfies the equation (adopts Einstein summation notation)

$$C_{ijkl}\frac{\partial^2 U_k}{\partial x_j \partial x_l} = \rho\frac{\partial^2 U_i}{\partial t^2}, \quad i,j,k,l = 1,2,3, \tag{A1}$$

where C_{ijkl} is the elastic constant tensor of the substrate, U_i is the displacement at the i direction, and ρ is the density of the substrate. Equation (A1) admits a plane-wave solution of

$$U_i = \tilde{U}_i \exp[i(\bar{k}\cdot\bar{x} - \omega t)], \tag{A2}$$

where $\tilde{U}_i$ is the unit polarization vector, $\bar{k} = 2\pi\bar{n}/\lambda$ is the wave vector, λ is the wavelength, and $\bar{n}$ is the wave normal. Putting Eq. (A2) back into Eq. (A1) gives the Christoffel equation,

$$\Gamma_{ik}\tilde{U}_k \equiv C_{ijkl}k_j k_l \tilde{U}_k = \rho\omega^2 \tilde{U}_i. \tag{A3}$$

Γ_{ik} is defined as the Christoffel matrix. For the eigenvalue problem of the 3×3 Christoffel matrix to have a solution, $\bar{k}$ and ω should have the following relationship:

$$\det(\Gamma_{ik} - \rho\omega^2\delta_{ik}) = 0. \tag{A4}$$

For SAW with wave vector $\bar{k}_\parallel = (k_1, k_2)$ and propagating on the (x_1, x_2) plane, the displacement $\bar{U}$ satisfies Eq. (A1). $\bar{U}$ can be written in Fourier space of $(\omega, \bar{k}_\parallel)$

$$U_i(\bar{x},t) = \frac{1}{(2\pi)^3}\int_{-\infty}^{\infty} d\bar{k}_\parallel \int_{-\infty}^{\infty} d\omega\, u_i(\bar{k}_\parallel, x_3, \omega) e^{i(\bar{k}_\parallel\cdot\bar{x}_\parallel - \omega t)}. \tag{A5}$$

With given ω and (k_1, k_2), Eq. (A4) can be solved to give six $k_3^{(n)}$ (possible complex numbers) and six corresponding eigenvectors $\bar{\alpha}^{(n)}$. According to linear algebra, they are components of the SAW. SAW should not have wave components that come from a substrate or with higher energy when deeper into a substrate. This selection rule eliminates three $k_3^{(n)}$ and corresponding $\bar{\alpha}^{(n)}$. With the three solutions left, the Fourier kernel in Eq. (A5) can be written as

$$u_i(\bar{k}_\parallel, x_3, \omega) = \sum_{n=1}^{3} A^{(n)}\alpha_i^{(n)} e^{ik_3^{(n)}x_3}, \tag{A6}$$

where $A^{(n)}$ are three coefficients of the linear combination of three wave components. They are the only unknowns.

Next, the boundary conditions are applied to solve the coefficients $A^{(n)}$. The boundary condition at surface $x_3 = 0$ is point excitation:

$$\sigma_{l3}(\bar{x}_\parallel, x_3 = 0, t) = C_{l3pq}\frac{\partial U_p(\bar{x}_\parallel, x_3 = 0, t)}{\partial x_q} = \delta_{l3}\delta(\bar{x}_\parallel)\delta(t), \tag{A7}$$

which can be written in Fourier space as

$$\delta_{l3}\delta(\bar{x}_\parallel)\delta(t) = \delta_{l3}\frac{1}{(2\pi)^3}\int_{-\infty}^{\infty} d\bar{k}_\parallel \int_{-\infty}^{\infty} d\omega\, e^{i(\bar{k}_\parallel\cdot\bar{x}_\parallel - \omega t)}. \tag{A8}$$

Applying Eqs. (A5), (A6), and (A8) in Eq. (A7), we have

$$\sum_{n=1}^{3} iC_{l3pq}k_q^{(n)}\alpha_p^{(n)}A^{(n)} = \delta_{l3}, \tag{A9a}$$

$$k_1^{(n)} = k_1, \quad k_2^{(n)} = k_2. \tag{A9b}$$

We can define the 3×3 matrix $B_l^{(n)} = iC_{l3pq}k_q^{(n)}\alpha_p^{(n)}$ and solve the equation $B_l^{(n)}A^{(n)} = \delta_{l3}$ to get all three $A^{(n)}$. Putting $A^{(n)}$ back into Eq. (A6) gives $\bar{u}(\bar{k}_\parallel, x_3, \omega)$. $\bar{u}(\bar{k}_\parallel, x_3 = 0, \omega)$ is the third column of the surface elastodynamic Green's function in Fourier space, G_{ij}, thus $G_{33} = u_3(\bar{k}_\parallel, x_3 = 0, \omega)$ can be obtained. $G_{33}(\bar{k}_\parallel, x_3 = 0, \omega)$ is mapped in $(k_\parallel, \omega)$ space (in the $\bar{k}_\parallel$ direction), and its extreme points define the dispersion curve. Figures 6(a) and 6(c) are the color maps of G_{33} close to the Brillouin zone center. Figure 10 is from the extreme points of G_{33}.

2. SAW of the substrate with a uniform mass layer

If there is a uniform layer on top of the substrate, the boundary condition becomes

$$\sigma_{l3}(x_\parallel, x_3 = 0, t) = C_{l3pq}\frac{\partial U_p(x_\parallel, x_3 = 0, t)}{\partial x_q} = \delta_{l3}\delta(x_\parallel)\delta(t) + \mu\frac{\partial^2 U_l(x_\parallel, x_3 = 0, t)}{\partial t^2}. \tag{A10}$$

Here μ is the mass per unit area. The mass loading term in Fourier space is

$$\mu\frac{\partial^2 U_l(x_\parallel, x_3 = 0, t)}{\partial t^2} = \frac{1}{(2\pi)^2}\int_{-\infty}^{\infty} dk_\parallel \int_{-\infty}^{\infty} d\omega\, e^{i(k_\parallel x_\parallel - \omega t)}(-\mu\omega^2) \times \sum_{n=1}^{3} A^{(n)}\alpha_l^{(n)} e^{ik_3^{(n)}(\bar{k}_\parallel,\omega)x_3}, \tag{A11}$$

$$k_1^{(n)} = k_1, \quad k_2^{(n)} = k_2, \quad k_3^{(n)} = k_3^{(n)}. \tag{A12}$$

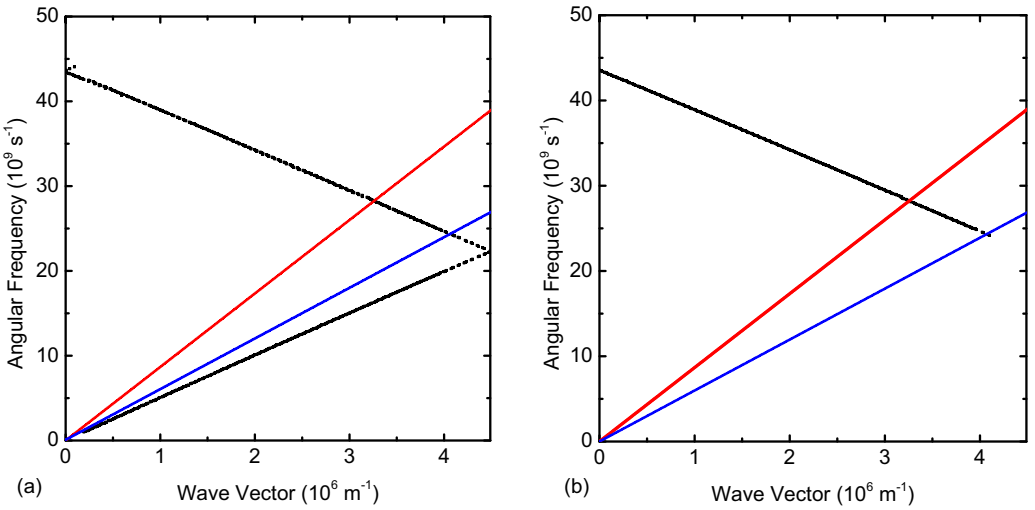

FIG. 10. Dispersion curve of the SAW from 0 to π/λ with metal grating, drawn by plotting extreme points of $G_{33}(k_\parallel, x_3 = 0, \omega)$. In both figures, the blue line is the dispersion curve of bulk fast transverse acoustic waves, and the red line is the dispersion curve of bulk longitudinal acoustic waves in the Si ⟨110⟩ direction; they are not from the $G_{33}(k_\parallel, x_3 = 0, \omega)$ calculation but are plotted separately. (a) The black line is $\mathrm{Re}(G_{33}(k_\parallel, \omega, x_3 = 0))$, which shows the mode folding and band structure in the first Brillouin zone. (b) The black line is $\mathrm{Im}(G_{33}(k_\parallel, \omega, x_3 = 0))$. The imaginary part of the Green's function appears only after the SAW couples with bulk acoustic waves. The acoustic band gap is too small to be visible in this plot.

So the boundary condition at $x_3 = 0$ is

$$\delta_{l3} = \sum_{n=1}^{3} A^{(n)} i C_{l3pq} \alpha_p^{(n)} k_q^{(n)} e^{ik_3^{(n)}(\bar{k}_\parallel,\omega)x_3} - (-\mu\omega^2) \sum_{n=1}^{3} A^{(n)} \alpha_l^{(n)} e^{ik_3^{(n)}(\bar{k}_\parallel,\omega)x_3} = \sum_{n=1}^{3} A^{(n)} \left[i C_{l3pq} \alpha_p^{(n)} k_q^{(n)} + \mu\omega^2 \alpha_l^{(n)} \right]. \quad \text{(A13)}$$

Using this new boundary condition and repeating the previous procedure, one can calculate G_{33}.

3. SAW of the substrate with periodic grating

Similarly, the periodic mass loading of metal grating changes the boundary condition to

$$\sigma_{l3}(x_\parallel, x_3 = 0, t) = C_{l3pq} \frac{\partial U_p(x_\parallel, x_3 = 0, t)}{\partial x_q} = \delta_{l3}\delta(x_\parallel)\delta(t) + \mu(x_\parallel) \frac{\partial^2 U_l(x_\parallel, x_3 = 0, t)}{\partial t^2} \quad \text{(A14)}$$

and $\mu(x_\parallel)$ has a periodic rectangular dependence on position (rectangular grating). Its Fourier transform is

$$\mu(x_\parallel) = \sum_{m=-\infty}^{\infty} \mu_m e^{imGx_\parallel}, \quad |\bar{G}| = \frac{2\pi}{\lambda} \quad \bar{G} = (g_1, g_2), \quad \text{(A15)}$$

where λ is the periodicity of the grating. When applying this boundary condition, $\mu(x_\parallel)$ causes the mixing between components $u_i(k_\parallel + nG, x_3, \omega)$, with integer n from $-\infty$ to ∞. So we rewrite the expression of surface displacement as

$$\begin{aligned} U_i(\bar{x}, t) &= \frac{1}{8\pi^3} \int_{-\infty}^{\infty} dk_\parallel \int_{-\infty}^{\infty} d\omega \, u_i(\bar{k}_\parallel, x_3, \omega) e^{i(k_\parallel x_\parallel - \omega t)} \\ &= \frac{1}{8\pi^3} \sum_{m=-\infty}^{\infty} \int_{-G/2}^{G/2} dk_\parallel \int_{-\infty}^{\infty} d\omega \, u_i(\bar{k}_\parallel + m\bar{G}, x_3, \omega) e^{i[(k_\parallel + mG)x_\parallel - \omega t]} \\ &= \frac{1}{8\pi^3} \int_{-G/2}^{G/2} dk_\parallel \int_{-\infty}^{\infty} d\omega \sum_{m=-\infty}^{\infty} u_i(\bar{k}_\parallel + m\bar{G}, x_3, \omega) e^{i[(k_\parallel + mG)x_\parallel - \omega t]} \\ &= \frac{1}{8\pi^3} \int_{-G/2}^{G/2} dk_\parallel \int_{-\infty}^{\infty} d\omega \sum_{m=-\infty}^{\infty} \sum_{n=1}^{3} A^{(n)(m)} \alpha_i^{(n)(m)} e^{ik_3^{(n)(m)} x_3} e^{i[(k_\parallel + mG)x_\parallel - \omega t]}. \end{aligned} \quad \text{(A16)}$$

$k_3^{(n)(m)}$ and $\alpha_i^{(n)(m)}$ correspond to the $(k_\parallel + mG_\parallel)$ term in the solution of the Christoffel equation. $\alpha_i^{(n)(m)}$ is independent with the size of $k_\parallel$; it only depends on the propagation direction. However, we still assign it to each m for the sake of programming the

calculation. A similar process can be applied for the boundary condition:

$$\delta_{l3}\delta(x_\parallel)\delta(t) = \delta_{l3}\frac{1}{(2\pi)^3}\int_{-\infty}^{\infty} dk_\parallel \int_{-\infty}^{\infty} d\omega\, e^{i(k_\parallel x_\parallel - \omega t)} = \delta_{l3}\frac{1}{(2\pi)^3}\int_{-G/2}^{G/2} dk_\parallel \int_{-\infty}^{\infty} d\omega \sum_{m=-\infty}^{\infty} e^{i[(k_\parallel + mG)x_\parallel - \omega t]}. \tag{A17}$$

In these integrals, we require $|k_\parallel| < G/2$. Therefore, the boundary condition is

$$\begin{aligned} & i\sum_{m=-\infty}^{\infty}\sum_{n=1}^{3} A^{(n)(m)} C_{3lpq}\alpha_p^{(n)(m)} k_q^{(n)(m)} e^{ik_3^{(n)(m)}x_3} e^{imGx_\parallel} \\ & = \delta_{l3}\sum_{m=-\infty}^{\infty} e^{imGx_\parallel} - \sum_{M=-\infty}^{\infty}\mu_M e^{iMGx_\parallel}\sum_{m=-\infty}^{\infty}\sum_{n=1}^{3}\omega^2 A^{(n)(m)}\alpha_l^{(n)(m)} e^{ik_3^{(n)(m)}x_3} e^{imGx_\parallel}. \end{aligned} \tag{A18}$$

Here we define $k_1^{(n)(m)} = k_1 + mg_1$, $k_2^{(n)(m)} = k_2 + mg_2$. Rearrange the index and apply $x_3 = 0$:

$$i\sum_{m=-\infty}^{\infty}\sum_{n=1}^{3} A^{(n)(m)} C_{3lpq}\alpha_p^{(n)(m)} k_q^{(n)(m)} e^{imGx_\parallel} = \delta_{l3}\sum_{m=-\infty}^{\infty} e^{imGx_\parallel} - \sum_{m=-\infty}^{\infty}\sum_{n=1}^{3}\omega^2\sum_{M=-\infty}^{\infty}\mu_M A^{(n)(m-M)}\alpha_l^{(n)(m-M)} e^{imGx_\parallel}, \tag{A19}$$

which will give the final relationship between all the coefficients of linear combination:

$$\sum_{m=-\infty}^{\infty} e^{imGx_\parallel}\sum_{n=1}^{3}\left[iA^{(n)(m)} C_{3lpq}\alpha_p^{(n)(m)} k_q^{(n)(m)} + \omega^2\sum_{M=-\infty}^{\infty}\mu_M A^{(n)(m-M)}\alpha_l^{(n)(m-M)}\right] = \delta_{l3}\sum_{m=-\infty}^{\infty} e^{imGx_\parallel}. \tag{A20}$$

It is clear that the harmonic terms in periodic mass loading cause the mixing between different eigenmodes. This is a linear algebra equation for all $A^{(n)(m)}$. It is impractical to consider all the harmonic terms. In our calculation, we only consider up to the fifth harmonics, i.e., we treat $A^{(n)(m)} = 0$ if $|m| > 5$. Solving all $A^{(n)(m)}$ can give $u_3(\bar{k}_\parallel, x_3 = 0, \omega)$.

Figure 10 is the dispersion curve of the SAW with the presence of metal grating. Re(G_{33}) shows the dispersion curve of the SAW. Figure 10(a) shows that the metal grating creates band structure. Im(G_{33}) represents the damping of the SAW. Figure 10(b) shows that the attenuation of the SAW by a metal grating is due to the coupling between the SAW and the bulk acoustic wave.

[1] H. J. Maris, in *Physical Acoustics*, edited by W. P. Mason and R. N. Thurston (Academic Press, New York, 1971), Vol. 8, pp. 279–345.
[2] K. L. Ekinci and M. L. Roukes, Rev. Sci. Instrum. **76**, 061101 (2005).
[3] R. Lifshitz and M. L. Roukes, Phys. Rev. B **61**, 5600 (2000).
[4] X. Sun, X. Zhang, and H. X. Tang, Appl. Phys. Lett. **100**, 173116 (2012).
[5] A. Akhiezer, J. Phys. (USSR) **1**, 277 (1939).
[6] T. O. Woodruff and H. Ehrenreich, Phys. Rev. **123**, 1553 (1961).
[7] H. J. Maris, Philos. Mag. **16**, 331 (1967).
[8] W. P. Mason and T. B. Bateman, J. Acoust. Soc. Am. **36**, 644 (1964).
[9] W. P. Mason, in *Physical Acoustics*, edited by W. P. Mason (Academic Press, New York, 1965), Vol. 3B, pp. 235–286.
[10] P. G. Klemens, in *Physical Acoustics*, edited by W. P. Mason (Academic Press, New York, 1965), Vol. 3B, pp. 201–234.
[11] H. J. Maris, Phys. Rev. **175**, 1077 (1968).
[12] H. E. Bömmel and K. Dransfeld, Phys. Rev. **117**, 1245 (1960).
[13] J. Lamb and J. Richter, Proc. R. Soc. London, Ser. A **293**, 479 (1966).
[14] S. Ghaffari, S. A. Chandorkar, S. Wang, E. J. Ng, C. H. Ahn, V. Hong, Y. Yang, and T. W. Kenny, Sci. Rep. **3**, 3244 (2013).
[15] J. Lamb, M. Redwood, and Z. Shteinshleifer, Phys. Rev. Lett. **3**, 28 (1959).
[16] B. G. Helme and P. J. King, Phys. Status Solidi A **45**, K33 (1978).
[17] K. Lücke, J. Appl. Phys. **27**, 1433 (1956).
[18] Y. V. Ilisavskii and V. M. Sternin, Sov. Phys. Solid State **27**, 236 (1985).
[19] K. R. Keller, J. Appl. Phys. **38**, 3777 (1967).
[20] B. C. Daly, K. Kang, Y. Wang, and D. G. Cahill, Phys. Rev. B **80**, 174112 (2009).
[21] O. Matsuda, O. B. Wright, D. H. Hurley, V. E. Gusev, and K. Shimizu, Phys. Rev. Lett. **93**, 095501 (2004).
[22] J. A. Rogers, A. A. Maznev, M. J. Banet, and K. A. Nelson, Annu. Rev. Mater. Sci. **30**, 117 (2000).
[23] A. A. Maznev, K. A. Nelson, and J. A. Rogers, Opt. Lett. **23**, 1319 (1998).
[24] D. Li, P. Zhao, J.-C. Zhao, and D. G. Cahill, J. Appl. Phys. **114**, 143102 (2013).
[25] H.-N. Lin, H. J. Maris, L. B. Freund, K. Y. Lee, H. Luhn, and D. P. Kern, J. Appl. Phys. **73**, 37 (1993).
[26] D. H. Hurley and K. L. Telschow, Phys. Rev. B **66**, 153301 (2002).
[27] T. Lee, K. Ohmori, C.-S. Shin, D. G. Cahill, I. Petrov, and J. E. Greene, Phys. Rev. B **71**, 144106 (2005).
[28] J. Andrew J. Slobodnik, Proc. IEEE **64**, 581 (1976).
[29] J. Andrew J. Slobodnik, J. Appl. Phys. **43**, 2565 (1972).
[30] S. Y. Chou, P. R. Krauss, and P. J. Renstrom, J. Vac. Sci. Technol. **14**, 4129 (1996).
[31] D. Chanda, K. Shigeta, S. Gupta, T. Cain, A. Carlson, A. Mihi, A. J. Baca, G. R. Bogart, P. Braun, and J. A. Rogers, Nat. Nanotechnol. **6**, 402 (2011).

[32] H. Schmid and B. Michel, Macromol. **33**, 3042 (2000).
[33] D. Nardi, M. Travagliati, M. E. Siemens, Q. Li, M. M. Murnane, H. C. Kapteyn, G. Ferrini, F. Parmigiani, and F. Banfi, Nano. Lett. **11**, 4126 (2011).
[34] R. Loudon and J. R. Sandercock, J. Phys. C **13**, 2609 (1980).
[35] K. Kang, Y. K. Koh, C. Chiritescu, X. Zheng, and D. G. Cahill, Rev. Sci. Instrum. **79**, 114901 (2008).
[36] A. G. Every, K. Y. Kim, and A. A. Maznev, J. Acoust. Soc. Am. **102**, 1346 (1997).
[37] G. W. Farnell, in *Physical Acoustics*, edited by W. P. Mason and R. N. Thurston (Academic Press, New York, 1970), Vol. 6, pp. 109–166.
[38] T. C. Lim and G. W. Farnell, J. Acoust. Soc. Am. **45**, 845 (1969).
[39] H. J. McSkimin, W. L. Bond, E. Buehler, and G. K. Teal, Phys. Rev. **83**, 1080 (1951).
[40] M. Tinkham, *Group Theory and Quantum Mechanics* (McGraw-Hill, New York, 1964).
[41] M. Hamermesh, *Group Theory and Its Application to Physical Problems* (Addison-Wesley, Reading, MA, 1962).
[42] B. Lüthi, *Physical Acoustics in the Solid State* (Springer-Verlag, Berlin, 2005).
[43] M. P. Brassington and G. A. Saunders, Phys. Rev. Lett. **48**, 159 (1982).
[44] H. J. Maris, Phys. Rev. **188**, 1308 (1969).
[45] H. J. Maris, Phys. Rev. B **28**, 7033 (1983).
[46] M. R. Hauser, R. L. Weaver, and J. P. Wolfe, Phys. Rev. Lett. **68**, 2604 (1992).
[47] A. A. Maznev and A. G. Every, J. Appl. Phys. **106**, 113531 (2009).
[48] Y. Touloukian and C. Ho, *Thermophysical Properties of Matter* (IFI/Plenum, New York, 1970).
[49] K. Yum, Z. Wang, A. P. Suryavanshi, and M.-F. Yu, J. Appl. Phys. **96**, 3933 (2004).
[50] Z. Hao, A. Erbil, and F. Ayazi, Sens. Actuators A **109**, 156 (2003).
[51] I. Wilson-Rae, Phys. Rev. B **77**, 245418 (2008).
[52] A. A. Kiselev and G. J. Iafrate, Phys. Rev. B **77**, 205436 (2008).
[53] S. D. Lambade, G. G. Sahasrabudhe, and S. Rajagopalan, Phys. Rev. B **51**, 15861 (1995).
[54] X. Zhang, J. D. Comins, A. G. Every, P. R. Stoddart, W. Pang, and T. E. Derry, Phys. Rev. B **58**, 13677 (1998).